Indian Journal of Pure & Applied Physics
Vol. 60, July 2022, pp. 600-609

Numerical Estimation of X-ray Emission from Europa and Dependence on Solar Activity

Smart Kundassery & C A Babu

Department of Atmospheric Sciences, School of Marine Sciences, Cochin University of Science and Technology, Kochi, Kerala-682 016, India

Received 27 February 2022; accepted 17 June 2022

Tenuous Europa is now known as an X-ray emitter. X-ray emission from a tenuous planetary object has an intricate connection to its surface composition. By taking into account the solar X-rays incident on its surface as the source of excitation of X-rays from the surface, models of probable surface composition, and physical processes leading to the generation of X-rays from the surface, we developed a numerical model to understand its X-ray emission. The model computes the solar X-ray flux at Europa distance during representative cases of a solar cycle (0.01–100 MK). Energetic photon-induced events leading to the emission of X-rays from the surface result from photoelectric absorption and scattering. Taking into account five representative phases of a solar cycle and four probable models of surface composition, we estimated the X-ray energy flux generated from the satellite and as observed by the Chandra X-ray Observatory (CXO). During the representative quiet to flare cases, the X-ray flux available at Europa for surface energetics varies from 4.63×10^{-8} to 3.23×10^{-4} ergs cm^{-2} s^{-1} (4.96 AU). Detectable X-ray energy flux from Europa at CXO varies from 5.27×10^{-22} to 9.44×10^{-20} ergs cm^{-2} s^{-1}. We also observed that the least energy flux is always emitted from the water-ice model of the surface composition. The presence of impurities in water-ice is seen as enhancing the X-ray emission from its veneer.

Keywords: Solar X-rays; Europa; Photoelectric absorption; Rayleigh Scattering; Veneer

1 Introduction

On airless planetary objects and natural satellites possessing tenuous atmospheres, the attenuation of the ever-pervasive photons of the solar electromagnetic spectrum (EM) occurs only from its regolith. The photons having energies greater than the binding energies of the elemental composition of the regolith can excite and even ionize the atomic constituents leading to the emission of X-ray photons from the regolith. Evaluation of the X-ray spectral emission signatures from the tenuous satellite following the energetic environment-surface interactions requires details of the source excitation and response events from the regolith. The regolith accounted for in this work is of the Jovian Europa, the satellite harbours a subsurface ocean[1], and we delineate in this work the energetic photon-induced emission of X-rays from the regolith of Europa.

As the excitation source of X-rays from Europa, we took into consideration the photons in the X-region of the EM spectrum of the Sun. In the EM spectrum, the X-region extends from wavelengths of ≈ 100–0.01 Å (≈100 eV–120 keV). Due to their penetrating abilities[2], X-rays in the high-energy region (≈12–120 keV) are known as hard X-rays [$\lambda < 1$ Å ($E > 12.4$ keV)], and the lower-end is referred to as soft X-ray region [$\lambda > 1$ Å ($E < 12.4$ keV)]. With h as the Planck's constant (6.6261×10^{-34} J.s), the energy E of the photon ($E = h.\nu = h.c.\lambda^{-1}$) is determined solely by the frequency (ν) or wavelength (λ) of the radiation. The solar X-rays originate from the corona. Since the energetic solar coronal X-rays have a dependence on the solar activity cycle, we also took into account the representative phases of a typical cycle of solar activity. The energetic photon-induced X-ray emission from the surface of the satellite, as detected by an orbiter in space, is indicative of the absorption and scattering process at the surface. The photon-induced response events from the surface of Europa attempted in this work consist of X-ray fluorescence (XRF) and scattering. The XRF occurs due to the photoelectric absorption of the incident energetic photons[3,4,5,6]. The photons in the energy range 0.7–10 keV (≈17.700–1.239 Å) undergo scattering from the regolith[7]. Scattering involves both Rayleigh and Compton scattering events, and these components generate a background continuum for the XRF line emission.

*Corresponding authors: (Email: babuca@cusat.ac.in)

In this context, for a comprehensive understanding of the energetic photon-induced surface energetics leading to the photon-induced response events from the surface of a tenuous natural satellite of the solar system harbouring a subsurface ocean, we developed a numerical model to quantify the sunshine and moonshine in X-rays from the satellite during representative phases of a typical cycle of solar activity. The salient details of the model which computes the source excitation fluxes, and the energy fluxes generated from the water-ice surface of Europa and received at the telescope of the Chandra X-ray Observatory (CXO) is already described in an earlier paper by the authors[8]. We now consider the impurities conglomerated into the water-ice matrix of the surface of Europa. Still considering the line and continuum emission process leading to the emission of X-rays from the Sun, we estimated the solar coronal energy flux at Europa during representative cases of a solar cycle. These estimates of the excitation fluxes are later used for the computation of the energetic photon-induced X-ray energy fluxes during the representative cases from the surface of Europa. Since the observed X-ray emission from Europa occurs in the soft X-ray range[9], we took into account only the X-ray fluorescent emission and the Rayleigh scattering for the estimation of the total energy flux from the satellite (ergs cm^{-2} s^{-1}).

The computed numbers of the solar X-ray flux at R = 1 AU are scaled to Europa distance as follows. X-ray emission from Europa was detected by CXO during its observation on November 25–26, 1999. Besides the photon-induced excitation of X-rays from the satellite, another probable mechanism leading to the emission of X-rays from the satellite is the particle-induced emission process. For the computation of the intensity of the energetic bombarding ions on Europa, observations of the EPD detector of Galileo mission flybys are available for three encounters[10]. During the E12 encounter on December 16, 1997, the average distance of Europa from the Sun was 5.52 AU, during the E19 encounter (February 1, 1999) was 5.59 AU, and during the E26 encounter (January 3, 2000) was 4.96 AU. For the aforementioned period of observation of CXO and among the encounters, the encounter E26 (January 3, 2000) was the closest to the period of observation of CXO (November 25–26, 1999). Consequently, to derive the relative significance of the photon and ion-induced X-ray emission from Europa, the photon-induced processes generated from the surface of Europa while the satellite was at a distance of 4.96 AU is undertaken.

This paper presents the significant features of the numerical model (§ 2), and for comparative estimates discusses the salient features of the X-ray energy flux received at the telescope of CXO (ergs cm^{-2} s^{-1}). The surface composition of Europa to which the energetic photons bestow an interaction (§ 2.1), the formalism and formulation of the photon-induced response events from the satellite (§ 2.2), and the salient results of the computed numbers are discussed (§ 3).

2 Materials and Methods

Solar X-ray photons are regarded in this work as the excitation source for the emission of X-rays from the surface of Europa. The source region of X-rays, the solar corona, is regarded as a typical case of low-density plasma, the plasma is a mixture of several different ions, the principal contributor among them is hydrogen, helium, and the solar coronal X-ray emission consists of line and continuum[11]. The line emission from a hot, dilute and optically thin low-density plasma results from the downward radiative transitions, and the emitted photon is resonance absorbed and re-emitted. Free-free emission, free-bound emission, and two-photon decay of the metastable states of hydrogen and helium lead to continuum emission, and we assume that the photon eventually escapes from hot plasma. We generated the solar X-ray energy flux during the representative conditions of a solar activity cycle (T_e = 1–100 MK) using the Chianti code (ergs cm^{-2} s^{-1}), and this flux is further used for the estimation of the solar coronal photon-induced response events from the satellite (ergs cm^{-2} s^{-1}). The probable solar coronal X-ray energy flux during these representative phases of the solar activity cycle and during the period of the observation of CXO is computed (1–100 Å), presented and discussed under the following premises.

The solar coronal thermal radiation is dependent upon electron temperature (T_e) and electron number density (N_e) through the emission measure ($N^2_e dV$). The representative numbers of the electron temperature (T_e) and the electron density (N_e) adopted for the computation of the probable solar X-ray flux at Europa distance during a solar cycle are as follows. The X-ray emission from an instant of coronal condition[12,13] is computed using T_e of 1.0 MK and an emission measure of 3.0×10^{49} cm^{-3} (SNo.1). The X-ray emission from an instant of general corona[12,14]

(SNo.2) is modelled using an electron temperature (T_e) of 1.5 MK and an emission measure of 3.0×10^{49} cm^{-3}. An instant of X-ray active region emission from the whole Sun[14] is also taken into account with an electron temperature (T_e) of 3.0 MK and an emission measure of 5.049×10^{49} cm^{-3} (SNo.3).

Apart from these scenarios, the predicted solar activity cycles from 1985–2020 reveal that the period of observation of CXO (November 25–26, 1999) belongs to the near maximum of the 23rd solar activity cycle[15]. The solar flux ($J(\lambda)$ ergs cm^{-2} s^{-1} keV^{-1}) during this period is computed by taking into account the solar flares. Solar flares are a short-lived sudden increase in the intensity of the radiation emitted in the neighbourhood of sunspots[15,16,17]. The GOES observation reveals that the dominant class of flares during the period of the observation of CXO were of C-class. We modelled the X-ray emission[18] due to a typical C-class [T_e = 12.0 MK and $N^2_e dV = 9.0 \times 10^{47}$ cm^{-3} (SNo.4)] and an M-class flare [T_e = 17.5 MK and $N^2_e dV = 7.0 \times 10^{48}$ cm^{-3} (SNo.5)]. Later, using these incident fluxes, we estimated the energy flux generated from the representative surface composition of Europa and received at the telescope of CXO.

2.1 Surface composition of Europa

The Jupiter system, a miniature solar system, consists of 79 known natural satellites as of today. Among them, the four largest and massive Galilean satellites are regular, and all others are irregular small shaped objects. Europa, the second-largest Galilean (radius = 1560.8 kilometres), is also the sixth-largest in the solar system, is tidally heated, geologically active and the thermal emission signatures from the surface show low latitude diurnal brightness temperatures[20] in the range of 86–132 K. The Doppler data generated with the radio carrier wave of Galileo mission measured the external gravitational field of Europa[21], and the measurements indicate a predominantly water ice-liquid outer shell of ≈100–200 kilometres thick. The measurements of the impact craters on the surface reveal that the floating ice shell is ≈19–25 kilometres thick[22,23]. The average age of the surface[24] is between 30–70 Myr, and the materials accumulate on the surface through endogenic and exogenic sources. The primary endogenic source is the subsurface ocean[1], resurfacing is known to occur[25], and the exogenic sources are the direct impacts of comets, asteroids, meteorites, micro-meteorites, the material ejected from the Jovian outer irregular satellites and the inner Io[26].

The major constituents on the surface are the water-ice and hydrated species. The presence of water-ice is indicated by the appearance of prominent vibrational bands in the spectra. Early infrared spectrometer tracings up to 2.5 μm revealed that the spectrum beyond 1.5 μm is reduced in intensity by a factor of 2–3. This observation was readily explained, later confirmed from the near-IR spectra[27] in the region 0.7–2.5 μm, by assuming a surface coverage of H_2O snow[28]. The 1–4 μm spectra also revealed large amounts of water-ice on the surface[29], the surface ice is predominantly amorphous and the ice at ≈1 mm depth is predominantly crystalline[30]. The reflectivity spectra of the trailing and leading sides of the Galilean satellites from airborne telescopic measurements[31] concluded that the leading side of Europa was almost entirely frost-covered with fractional coverage > 85%. The spectrum of the trailing side of Europa at 1.5–2.0 μm absorptions is very asymmetric compared to those for water frost[32], and minerals are the probable source[33]. The Near Infrared Mapping Spectrometer (NIMS) of the Galileo orbiter returned infrared reflectance spectra exhibiting asymmetric absorption bands in the 1–3 μm spectral regions[34]. The primary features in this region are attributed to the water-ice overtones that shift in frequency and become asymmetric when ice contains impurities. On Europa, these asymmetric spectral signatures are seen as concentrated in lineaments and chaotic terrain[35,36].

The ubiquitous water-ice and its amorphous low-density phase is taken in this work as the Model-A. The direct comparison of the diffuse reflectance spectra of flash-frozen $MgSO_4$ (magnesium sulfate), Na_2SO_4 (sodium sulfate) and H_2SO_4 (sulphuric acid) with ratios 0.50:0.25:0.25 (mole-percent) has given near perfect matches to NIMS data[37]; $NaHSO_4$ (sodium bisulfate) rather than equal amounts of Na_2SO_4 and H_2SO_4 is also possible. A linear mixture model using cryogenic laboratory spectra as end members consisting of 14% hexahydrite, 11% bloedite, 12% mirabilite and 63% sulphuric acid hydrate is also probable[38]. An excellent fit is also 35.4% sulphuric acid hydrate, 18.2% hexahydrite, 17.9% mirabilite, 7.7% 100 μm grains of ice and 20.6% 250 μm grains of ice[39]. Besides the predominant water-ice composition (Model-A), we used these aforementioned propositions[37,38,39] to take into account the presence of impurities interspersed in the water-ice regolith, and formulated four probable elemental composition models of the surface of

Europa (Table 1). Subsequently, Model-B/C depict an endogenic source[37], Model-D depict an exogenic source[38] and Model-E is a generalized representative model[39], and all these models conform to the Galileo NIMS data.

The elemental composition of these most probable models (Table 2) is hydrogen (Z = 1), oxygen (Z = 8), sodium (Z = 11), magnesium (Z = 12), sulphur (Z = 16), and; except for hydrogen, all others have fluorescent emission (Table 3). In the water-ice (Model-A), oxygen has the dominant mass fraction (C_z = 0.888), is the only fluorescing element, has a K-edge (E_K) at 0.525 keV, and the oxygen K_α emission occurs at 0.537 keV. The Model-B/C through Model-E has hydrogen, oxygen, sodium, magnesium and sulphur as its elemental composition. Our computations reveal that in Model-B/C, oxygen (0.53) has the dominant mass fraction followed by sulphur (0.27), magnesium (0.10), sodium (0.096) and hydrogen (4.19E-03). In Model-D, oxygen (0.68) has the dominant mass fraction followed by sulphur (0.23), hydrogen (0.04), sodium (0.03) and magnesium (0.02). In Model-E, oxygen (0.75) has the dominant mass fraction followed by sulphur (0.14), hydrogen (0.07), sodium (0.03) and magnesium (0.02). These probable elemental compositions of the models of the surface composition of Europa are further used for the estimation of the X-ray energy flux generated from the surface due to the energetic photon-induced absorption and scattering events.

Table 1 — Constituents of various models of Europa's surface composition.

Model-A	**Mass%**
LDA Water-ice LDA H_2O ice	100%
Model-B[37]	**Mol%**
Magnesium sulfate $MgSO_4$	0.50
Sodium sulfate Na_2SO_4	0.25
Sulphuric acid H_2SO_4	0.25
Model-C[37]	**Mol%**
Magnesium sulfate $MgSO_4$	0.50
Sodium bisulfate $NaHSO_4$	0.50
Model-D[38]	**Mass%**
Sulphuric acid hydrate H_4O_5S	63.0
Hexahydrite $MgSO_4.6(H_2O)$	14.0
Mirabilite $Na_2SO_4.10(H_2O)$	12.0
Bloedite $Na_2Mg(SO_4)_2.4(H_2O)$	11.0
Model-E[39]	**Mass%**
Sulphuric acid hydrate H_4O_5S	35.4
Water-ice H_2O	28.3
Hexahydrite $MgSO_4.6(H_2O)$	18.2
Mirabilite $Na_2SO_4.10(H_2O)$	17.9

Notes. - LDA stands for Low Density Amorphous phase of water-ice. The constituents specified in these models are used to compute the fractional percentage of the elemental constituents of the probable models of the surface of Europa (Table 2).

2.2 Photons and Photon-induced response events

2.2.1 X-ray fluorescence

The production of X-ray fluorescent photons from a tenuous planetary regolith result from the interaction of the solar X-ray photons with their elemental composition. Ionization is the process by which the electrons are lost from or transferred to neutral molecules or atoms to form positively or negatively charged-particles. The photoelectric effect, the simplest example of photo-ionization, is possible only if the energy of the incoming photon is at least as large as the binding energy (B) of the electron in one of the states of the atomic shell, the ejected electron (photo-electron) from an atomic shell emerge with kinetic energy T (= h.ν – B), and results in the creation of a hole or a vacancy leading to the sustenance of an

Table 2 — Fractional percentage of elements in Europa's surface composition.

Element/Model	Water-ice	Model-B/C[37]	Model-D[38]	Model-E[39]
Hydrogen	11.20	0.42	3.95	6.49
Oxygen	88.80	53.24	67.89	74.87
Sodium	-	9.56	3.23	2.58
Magnesium	-	10.11	2.29	1.94
Sulphur	-	26.74	22.67	14.14

Table 3 — Tabulated parameters used for computation.

Element	Atomic Mass[40] A_Z (g mol^{-1})	Fluorescence yield[41] $\omega_{K,Z}$	Fluorescent energy[42] K_α (keV)	K-edge[43] E_K (keV)
Oxygen	15.999	0.008	0.525	0.537
Sodium	22.990	0.023	1.041	1.072
Magnesium	24.304	0.030	1.254	1.305
Sulphur	32.059	0.078	2.308	2.472

Notes. - Notation Z denote the atomic number of an element.

excited state. It must lose a specific amount of energy to occupy the closer shell of more binding energy. This excess energy appears as a photon whose energy is the difference between the binding energies of the filled outer-shell and the vacant inner-shell (radiative transition). The emission occurs in the X-region of the EM spectrum, the X-rays produced in this manner are called characteristic X-rays, the energy spectrum emitted by this process is specific to the particular atomic species involved, and acts as a fingerprint of the elements. This process of emission of characteristic photons after the photo-absorption is known as X-ray Fluorescence (XRF).

With J(λ) as the incident solar coronal X-ray energy flux computed in the wavelength interval, C_i as the mass fraction or concentration of each element in the elemental composition of the surface, C_j that of the fluorescing element, A_i denotes its relative atomic mass, the intensity (I) of the X-ray fluorescence I generated from a surface[5] is computed by integrating from a minimum wavelength (λ_{min}) above which the fluorescence is determined to become negligible to the K absorption edge (λ_K) as:

$$I_j(\lambda) = C_j \omega_j g_j J_K \frac{d\Omega}{4\pi D^2} \times \int_{\lambda_{min}}^{\lambda_K} \frac{J(\lambda)\cos(\alpha)\mu_{j_\lambda}}{\Sigma_i \left[C_i\mu_i(\lambda) + C_i\mu_i(\lambda_j)\frac{\cos(\alpha)}{\cos(\beta)}\right]} \mathrm{dE} \quad \ldots (1)$$

The various terms appearing in this expression can be understood in terms of the parameters that characterize the source excitation flux, the detector and the surface composition of the medium. The source excitation flux is the solar coronal X-rays, the flux J(λ) in the wavelength interval has units of ergs cm^{-2} s^{-1} $Å^{-1}$ (1–100 Å), and the flux J(E) in the energy interval has units of ergs cm^{-2} s^{-1} keV^{-1} (0.1–12.4 keV). The solid angle of the detector of the sensor is denoted as dΩ, the generation of fluorescence is statistically isotropic, is independent of the emission angle, is divided by 4π to obtain the yield per unit solid angle, and D is the distance from the Sun (AU). The notation α denote the incident angle of the primary X-rays to the normal (0^o at the sub-solar point). The strength of the source depends on the complement of the incident flux angle of the source. Thus, J(λ) is multiplied by the cosine of α, and β is the complement of the exiting flux angle (0^o for nadir-pointing).

The elemental composition of the surface is characterized in the expression through the parameters c_i, c_j (mass fraction), ω_j (fluorescence yield), g_j (transition probability), r_j (absorption jump ratio) and μ (absorption/attenuation coefficients). We obtained the current numbers of ω_K, $g_{K\alpha}$ and r_K from the database xraylib[44]; K absorption edge energies (E_K) and the characteristic wavelength (K_α) of the elemental composition from literature[42,43], and the absorption/ attenuation coefficients (μ cm^2 g^{-1}) are computed using the NIST XCOM photon cross section database[45]. These descriptions of the source flux and the medium are also applicable for the characterization of the surface for the computation of the Rayleigh scattering and the total energy flux generated from the surface.

2.2.2 Rayleigh scattering

The scattering is a process in which a free charge radiates in response to an incident EM wave. Rayleigh scattering is the process by which the incident photons are elastically scattered by the bound atomic electrons, the atom is neither ionized nor excited, its energy remains unaltered, and the incident photon is recoiled by the entire atom changing thereby its momentum and polarization. As a result, the energy of the scattered photon is identical to that of the incident photon, the photon is scattered by the combined action of the whole atom, and hence, the scattering is coherent. In the energy range 10–100 keV, the cross section for the Rayleigh scattering of X-rays compete with that for incoherent scattering (Compton). The model equation for the computation of the Rayleigh scatter $\sigma_R(\lambda)$ at a particular wavelength[5,6,7], formulated on the assumption that the surface has a 'homogeneous interior' and is much 'thicker than the interaction length of an X-ray photon', is:

$$\sigma_R(\lambda) = \xi_i \frac{d\Omega}{4\pi D^2} \times \int_{E_{min}}^{E_{max}} \frac{\Sigma_i^N J(\lambda)\cos(\alpha)\frac{C_i}{A_i}}{\Sigma_i^N \left[\mu_i(E_i)\left(1+\frac{\cos(\alpha)}{\cos(\beta)}\right)\right]} dE \quad \ldots (2)$$

As the energy of the incident photon increases, the electron is no longer a classical point charge. With x as the momentum transfer variable, Z as the atomic number of the nucleus of the target atom, the modification to correct the point charge formula of Thomson for an extended charge distribution is described by the atomic form factor F(x, Z). F^2(x, Z) is the probability that Z electrons of an atom take up the recoil momentum (x) without absorbing any energy. With A_i as the atomic weight of the absorber i,

N_A (6.022×10^{23} mol^{-1}) as the Avogadro's number, r_e (2.818×10^{-15} cm) as the classical radius of the electron[46], θ as the scattering angle, $d_e\sigma_{Th}/d\Omega$ as the electronic DCS per unit solid angle for the Thomson scattering of an unpolarized radiation on a free electron (cm^2/electron/steradian), $d_a\sigma_R/d\Omega$ as the Rayleigh DCS for the elastic scattering of unpolarized photons, the efficiency factor of the Rayleigh scattering[7] ξ_i is computed as:

$$\xi_i = \frac{N_A}{A_i}\frac{da_R^\sigma}{d\Omega}$$

$$\frac{d\,a_R^\sigma}{d\Omega} = \frac{de_{th}^\sigma}{d\Omega}\,[F(x,Z)]^2 = \frac{r_e^2}{2}\,(1+\cos^2\theta)[F(x,Z)]^2 \quad \ldots (3)$$

In order to eliminate the need for the interpolation of the tables of the computed form factors in literature[47], an exponential fit as an analytical function is available[48]. We used this function with the notation θ denoting the Bragg angle (half the take-off angle of the spot), λ denoting the wavelength in Å in the range of the scattering vectors between $0 < (\sin\theta)/\lambda < 2.0$ $Å^{-1}$ to compute the atomic form factor using a_i, b_i and c as the Cromer Mann coefficients as:

$$f^o sin\frac{\theta}{\lambda} = \Sigma_{i=1}^{4}\,[a_i \exp\,(-b_i\left[\frac{\sin(\theta)}{\lambda}\right]^2)] \quad \ldots (4)$$

As in eq. 1, the various terms appearing in this expression can be understood in terms of the parameters that characterize the source excitation flux J(λ), detector ($d\Omega/4\pi D^2$), parameters that characterize the elemental composition of the surface (C_i, A_i, μ_i, ξ_i). The explanatory notes given for the parameters in eq. 1 is also valid for eq. 2.

3 Results and Discussions

3.1 Solar coronal X-ray emission flux over a solar cycle

The integrated numbers of the solar X-ray flux J(E) (ergs cm^{-2} s^{-1}) modelled with Chianti in the energy interval (0.1–12.4 keV) during the representative conditions of a solar cycle (SNo.1–5) while Europa is at 4.96 AU are presented (Table 4). An instant of X-ray emission from a coronal condition modelled using an electron temperature (T_e) of 1.0 MK and an electron density (N_e) of 14.57×10^7 cm^{-3} generates an X-ray energy flux of 2.95×10^{-4} ergs cm^{-2} s^{-1} (SNo.1) at Europa distance. An instant of general corona [T_e = 1.5 MK; N_e = 14.56×10^7 cm^{-3}] generates an X-ray energy flux of 3.23×10^{-4} ergs cm^{-2} s^{-1} (SNo.2). An instant of X-ray active region emission from the whole Sun [T_e = 3.0 MK; N_e = 5.98×10^7 cm^{-3}] generates an X-ray energy flux of 3.85×10^{-5} ergs cm^{-2} s^{-1} (SNo.3). A typical C1-class of flare [T_e = 12.0 MK; N_e = 2.52×10^7 cm^{-3}] generates 9.24×10^{-6} ergs cm^{-2} s^{-1} (SNo.4). A typical M1-class of flare [T_e = 17.5 MK; N_e = 7.04×10^7 cm^{-3}] generates 4.23×10^{-5} ergs cm^{-2} s^{-1} (SNo.5). Apart from these computed results, during the quiet solar conditions, the solar flux at 1 AU in the X-ray range[19] is equal to 10^{-9} J m^{-2} s^{-1} and hence, the probable X-ray energy flux during the quiet condition at 4.96 AU is 4.63×10^{-8} ergs cm^{-2} s^{-1}. A closer look at Fig. 1, which depicts the solar coronal X-ray energy flux at Europa distance (4.96 AU), also reveals that even the

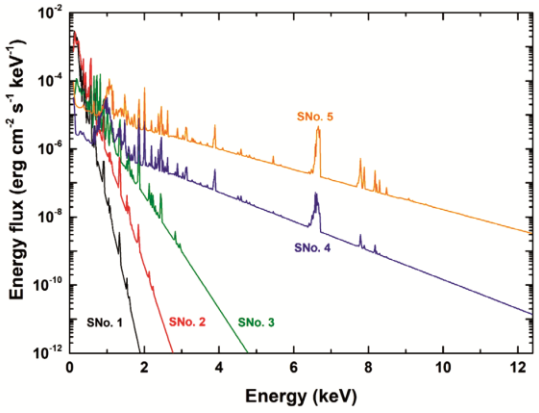

Fig. 1 — Solar coronal X-ray energy flux at Europa distance (4.96 AU).

Table 4 — Solar coronal X-ray energy flux at Europa distance (4.96 AU).

Solar Condition	T_e (MK)	N_e (10^7 cm^{-3})	Energy Flux (erg cm^{-2} s^{-1})
SNo.1	1.00	14.57	2.95E-04
SNo.2	1.50	14.56	3.23E-04
SNo.3	3.00	5.980	3.85E-05
SNo.4	12.0	2.520	9.24E-06
SNo.5	17.5	7.040	4.23E-05

Notes. - The solar coronal X-ray fluxes in the energy interval at 4.96 AU during the representative phases of a solar activity cycle. SNo.1 provide the fluxes for a typical case of coronal condition[12]; SNo.2 provides the fluxes for a case of general corona[12,14]; SNo.3 provide the fluxes for a case of X-ray active region emission from the whole Sun[19]; SNo.4–5 provide the fluxes for two cases of GOES solar flares (C1- and M1-class of flares).

flux generated by the solar coronal condition SNo.2 onwards can cause fluorescent emission from the probable five-elemental representative composition of the models of the surface composition of Europa addressed in this work. Also, the flux generated by the solar conditions SNo.1–3 is seen as considerably higher in the lower energy ranges than seen during the flare conditions (SNo.4–5).

It is deducted that during all these representative cases of the solar cycle, the solar coronal X-ray flux in the energy interval available at 4.96 AU for driving its surface energetics leading to the emission of X-rays from Europa can vary from 4.63×10^{-8} to 3.23×10^{-4} ergs cm^{-2} s^{-1}. We have used these estimates of the solar coronal X-ray energy fluxes available at Europa distance of 4.96 AU to gain insights into the probable levels of X-ray energy flux during the representative phases of a solar activity cycle. The estimates of the photon-induced XRF, and the total (XRF + Rayleigh) energy fluxes during these representative conditions of the solar cycle are as follows.

3.2 Probable XRF, Rayleigh and Total fluxes at CXO during a solar cycle

During a typical solar condition (SNo.1), the computed oxygen K_α emission flux received at CXO from the water-ice composition of Europa (Model-A) is 2.01E-18 ergs cm^{-2} s^{-1}. From Model-B/C, the K_α energy flux (ergs cm^{-2} s^{-1}) due to sodium is found lower (5.66E-20), and enhances through magnesium (1.13E-19), oxygen (1.67E-18) and sulphur (2.02E-18). From Model-D, the K_α energy flux due to sodium (1.60E-20) is found lower, and enhances through magnesium (2.15E-20), sulphur (1.43E-18) and oxygen (1.79E-18). From Model-E, the K_α energy flux due to sodium (1.20E-20) is found lower, and enhances through magnesium (1.71E-20), sulphur (8.41E-19) and oxygen (1.85E-18).

In the case of a general corona with one active region (SNo.2), from the water-ice, the oxygen K_α energy flux is 2.04E-18 ergs cm^{-2} s^{-1}. From Model-B/C, the K_α energy flux due to sodium (7.44E-20) is found lower, and enhances through magnesium (1.50E-19), oxygen (1.70E-18) and sulphur (2.73E-18). From Model-D, the K_α energy flux due to sodium (2.12E-20) is found lower, and enhances through magnesium (2.87E-20), oxygen (1.83E-18) and sulphur (1.96E-18). From Model-E, the K_α energy flux due to sodium (1.60E-20) is found lower, and enhances through magnesium (2.31E-20), sulphur (1.16E-18) and oxygen (1.89E-18).

In the case of X-ray active region emission from the whole Sun (SNo.3), from the water-ice, the energy flux is 1.27E-19 ergs cm^{-2} s^{-1}. From Model-B/C, the K_α energy flux due to sodium (1.10E-20) is found lower, and enhances through magnesium (2.30E-20), oxygen (1.04E-19) and sulphur (4.72E-19). From Model-D, the K_α energy flux due to sodium (3.20E-21) is found lower, and enhances through magnesium (4.58E-21), oxygen (1.12E-19) and sulphur (3.53E-19). From Model-E, the K_α energy flux due to sodium (2.45E-21) is found lower, and enhances through magnesium (3.75E-21), oxygen (1.17E-19) and sulphur (2.12E-19).

During the typical solar flares, from the water-ice, the oxygen K_α energy flux during C1-flare (SNo.4) and M1-flare (SNo 5) are 1.19E-20 ergs cm^{-2} s^{-1} and 5.21E-20 ergs cm^{-2} s^{-1} respectively. From Model-B/C, the K_α energy flux (SNo.4) due to sodium (1.89E-21) is found lower, and enhances through magnesium (4.18E-21), oxygen (8.15E-21) and sulphur (1.08E-19). The K_α energy flux (SNo.5) due to sodium (6.55E-21) is found lower, and enhances through magnesium (1.45E-20), oxygen (3.77E-20) and sulphur (4.02E-19). From Model-D, the K_α energy flux (SNo.4) due to sodium (5.60E-22) is found lower, and enhances through magnesium (8.72E-22) and sulphur (8.63E-20). The K_α energy flux (SNo.5) due to sodium (1.95E-21) is found lower, and enhances through magnesium (3.04E-21), oxygen (4.17E-20) and sulphur (3.34E-19). From Model-E, the K_α energy flux (SNo.4) due to sodium (4.33E-22) is found lower, and enhances through magnesium (7.21E-22), oxygen (9.56E-21) and sulphur (5.26E-20). The K_α energy flux (SNo.5) due to sodium (1.51E-21) is found lower, and enhances through magnesium (2.51E-21), oxygen (4.39E-20) and sulphur (2.04E-19).

The Rayleigh spectrum from four models of the surface composition (Figs 2–5) reveals that beyond 8.5 keV, the scattering is seen as nil. Throughout the energy spectrum, the scattering caused by the M-class flare (SNo.5) is seen as dominant. The lower energy ranges are dominated by the case of general corona (SNo.2) and the case of X-ray active region emission from the whole Sun (SNo.3). The Rayleigh spectrum of Model-D and Model-E are seen as almost similar.

The spectra in the energy interval (ergs cm^{-2} s^{-1} keV^{-1}) generated by the Rayleigh scattering (Figs 2-5), and the total (XRF + Rayleigh) energy flux generated from Model-A (Fig. 6), Model-B/C (Fig. 7),

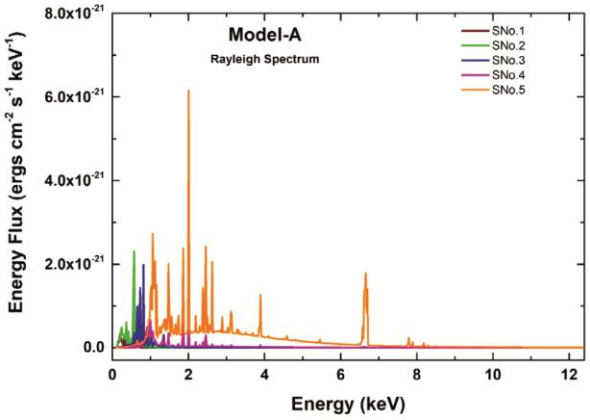

Fig. 2 — Rayleigh spectrum received at CXO from Europa's Model-A (water-ice) composition.

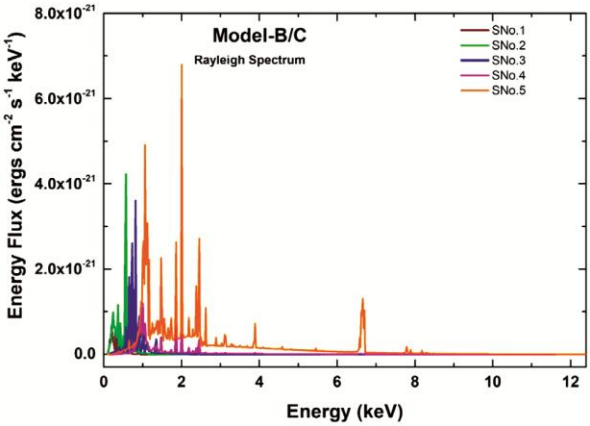

Fig. 3 — Rayleigh spectrum received at CXO from Europa's Model-B/C composition.

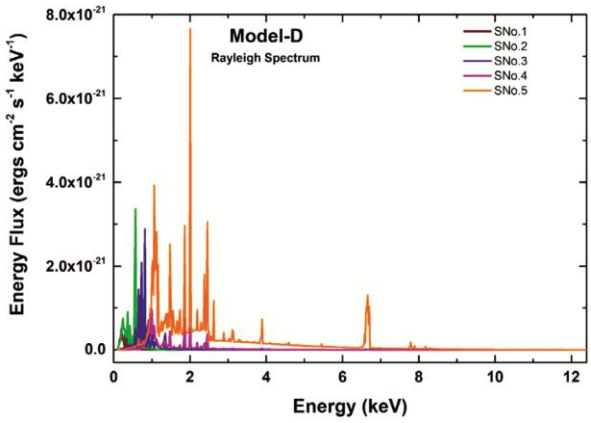

Fig. 4 — Rayleigh spectrum received at CXO from Europa's Model-D composition.

Model-D (Fig. 8) and Model-E (Fig. 9) surface of Europa at 4.96 AU and received at CXO are as follows. During the coronal condition (SNo.1), the energy flux (ergs cm^{-2} s^{-1}) from the water-ice received at CXO is 4.12E-20, from Model-B/C is

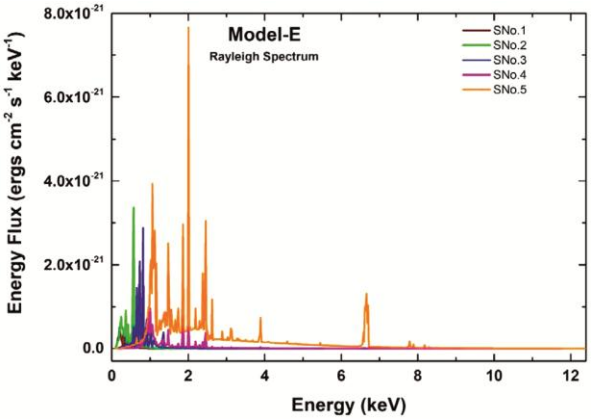

Fig. 5 — Rayleigh spectrum received at CXO from Europa's Model-E composition.

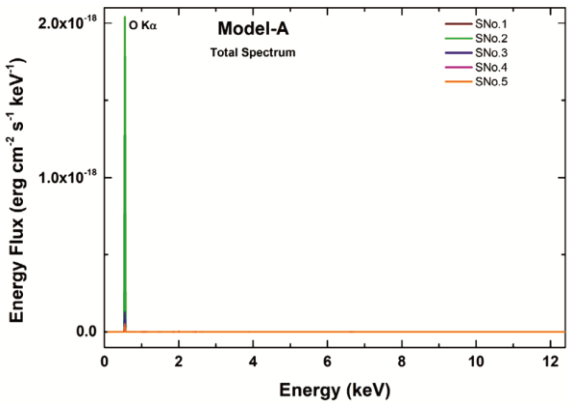

Fig. 6 — Total X-ray spectrum (XRF + Rayleigh) at CXO from Europa's Model-A composition.

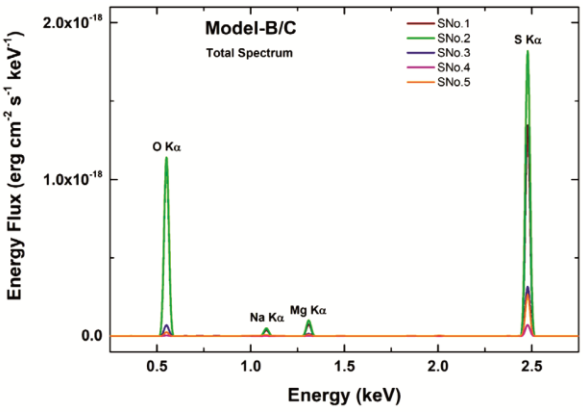

Fig. 7 — Total X-ray spectrum (XRF + Rayleigh) at CXO from Europa's Model-B/C composition.

7.81E-20, from Model-D is 6.62E-20, from Model-E is 5.54E-20. For general corona with one active region (SNo.2), the energy flux from the water-ice is 4.19E-20, from Model-B/C is 9.44E-20, from Model-D is 7.79E-20 and from Model-E is 6.30E-20. For the case of X-ray active region emission from the whole

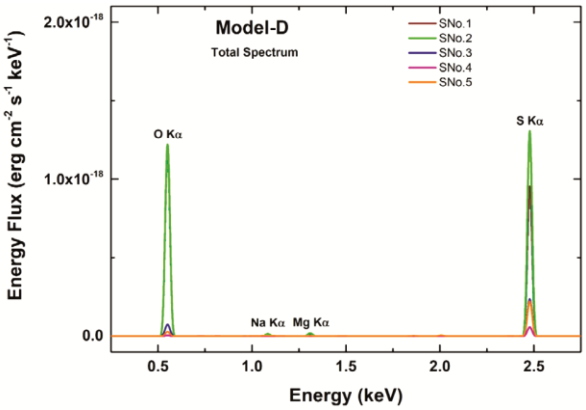

Fig. 8 — Total X-ray spectrum (XRF + Rayleigh) at CXO from Europa's Model-D composition.

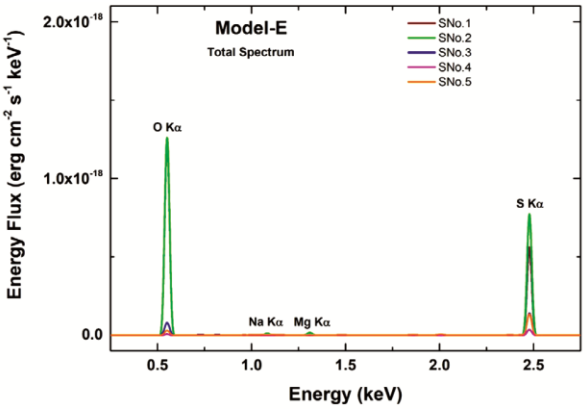

Fig. 9 — Total X-ray spectrum (XRF + Rayleigh) at CXO from Europa's Model-E composition.

sun (SNo.3), the energy flux from the water-ice is 2.83E-21, from Model-B/C is 1.27E-20, from Model-D is 9.84E-21 and from Model-E is 7.10E-21. For the case of solar flares (SNo.4–5), the energy flux from the water-ice ranges from 5.27E-22 to 3.56E-21, from Model-B/C range from 2.80E-21 to 1.16E-20 (SNo.4–5), from Model-D range from 2.28E-21 to 1.00E-20 (SNo.4–5) and from Model-E range from 1.61E-21 to 7.45E-21 (SNo.4–5). It is also observed that the least energy flux is always emitted from the water-ice (Model-A), and is seen as enhancing through Model-E, Model-D (exogenic representation of the surface composition) and Model-B/C (endogenic representation of the surface composition).

From all models of the probable surface composition of Europa (Figs 6–9), higher total X-ray emission flux is always generated by the case of general corona (SNo.2). From the predominant water-ice composition (Model-A), the emission flux from the surface diminishes through the case of X-ray active region emission from the whole Sun (SNo.3) and the least flux is caused by an M-class flare (SNo.5). From Model-B/C, the flux diminishes through the general case of solar condition (SNo.1), X-ray active region emission from the whole Sun (SNo.3), M-class flare (SNo.5) and least flux is caused by the C-class flare (SNo.4). From all models of the surface composition, the sulphur K_α contribution to emission is seen higher and diminish through oxygen K_α, magnesium K_α and sodium K_α. A similar profile as seen in Model-B/C is also seen as prevailing from Model-D and Model-E. The oxygen K_α from Model-A is seen as higher than generated from Model-B/C, Model-D and Model-E. The fluxes due to sodium K_α and magnesium K_α is seen as lower in Model-D, enhance through Model-E and is seen as higher in Model-B/C. The fluxes due to sulphur K_α are seen as higher in Model-B/C, and diminish through Model-D and Model-E.

4 Conclusions

It is deducted that the energetic solar coronal X-ray photon-induced X-ray emission during the representative cases of a solar activity cycle flux (ergs cm^{-2} s^{-1}) generated from the water-ice composition of the surface of Europa (Model-A) varies from 5.27E-22 to 4.19E-20, from Model-B/C from 2.80E-21 to 9.44E-20, from Model-D from 2.28E-21 to 7.79E-20, and from Model-E from 1.61E-21 to 6.30E-20. Detectable total (XRF + Rayleigh) X-ray energy flux from Europa at CXO varies from 5.27E-22 to 9.44E-20 ergs cm^{-2} s^{-1}. These numbers indicate that the least flux from all probable models of the surface composition of Europa is generated during the solar condition of flares (SNo.4) and maximum flux during a case of X-ray emission from the general corona (SNo.2).

It is thus observed that during the representative cases of a coronal condition (SNo.1), the total energy flux (ergs cm^{-2} s^{-1}) generated from the probable models of the surface composition of Europa varies from 4.12E-20 to 7.81E-20, for a general corona with one active region varies from 4.19E-20 to 9.44E-20 (SNo.2), for the X-ray active region emission from the whole Sun varies from 2.83E-21 to 1.27E-20 (SNo.3), for a C-class flare varies from 5.27E-22 to 2.80E-21 (SNo.4) and for an M-class flare varies from 3.56E-21 to 1.16E-20 (SNo.5). We still note that these numbers are still seen as far less than the numbers observed by CXO (3.0×10^{-16} ergs cm^{-2} s^{-1}), and requires more energetic sources to generate higher fluxes from the surface of Europa.

Acknowledgments

Smart Kundassery is supported by the Junior (Cochin University of Science and Technology and PURSE Programme of Department of Science and Technology, India) and Senior (ISRO-PLANEX) Research Fellowship during the period of this work.

References

1 Carr M H, Belton M J S, Chapman C R, Davies M E, Geissler P, Greenberg R, McEwen A S, Tufts B R, Greeley R, Sullivan R, Head J W, Pappalardo R T, Klaasen K P, Johnson T V, Kaufman J, Senske D, Moore J, Neukum G, Schubert G, Burns J A, Thomas P & Veverka J, *Nature*, 391 (1998) 363.
2 de Jager C, *Symp - Int Astronom Union*, 23 (1965) 45.
3 Adler I, Trombka J, Gerard J, Lowman P, Schmadebeck R, Blodget H, Eller E, Yin L, Lamothe R, Gorenstein P & Bjorkholm P, *Science*, 175 (1972) 436.
4 Adler I, Trombka J I, Schmadebeck R, Lowman P, Blodget H, Yin L, Eller E, Podwysocki M, Weidner J R, Bickel A L, Lum R K L, Gerard J, Gorenstein P, Bjorkholm P & Harris B, *Lunar Planet Sci Conf Proc*, (1973) 2783.
5 Clark P E, & Trombka J I, *J Geophys Res Planets*, 102 (1997) 16361.
6 Banerjee D & Vadawale S, *Adv Space Res*, 46 (2010) 651.
7 Ogawa K, Okada T, Shirai K & Kato M, *Earth Planets Space*, 60 (2008) 283.
8 Smart K B & Babu C A, *Indian J Pure Appl Phys*, 60 (2022) 16.
9 Elsner R F, Gladstone G R, Waite J H, Crary F J, Howell R R, Johnson R E, Ford P G, Metzger A E, Hurley K C, Feigelson E D, Garmire G P, Bhardwaj A, Grodent D C, Majeed T, Tennant A F & Weisskopf M C, *Astrophys J*, 572 (2002) 1077.
10 Paranicas C, Ratliff J M, Mauk B H, Cohen C & Johnson R E, *Geophys Res Lett*, 29 (2002) 18.
11 Tucker W H & Koren M, *Astrophys J*, 168 (1971) 283.
12 Elwert G, *J Geophys Res*, 66 (1961) 391.
13 Slemzin V A, Goryaev F F & Kuzin S V, *Plasma Phys Rep*, 40 (2014) 855.
14 Culhane J L, *Mon Not R Astron Soc*, 144 (1969) 375.
15 Hathaway D H, *Living Rev Sol Phys*, 12 (2015).
16 Carrington R C, *Mon Not R Astron Soc*, 20 (1859) 13.
17 Hodgson R, *Mon Not R Astron Soc*, 20 (1859) 15.
18 Feldman U, Doschek G A, Mariska J T & Brown C M, *Astrophys J*, 450 (1995) 441.
19 Banks & Cokarts, *Aeronomy*, (Elsevier), 1973.
20 Spencer J R, Tamppari L K, Martin T Z & Travis L D, *Science*, 284 (1999) 1514.
21 Anderson J D, Schubert G, Jacobson R A, Lau E L, Moore W B & Sjogren W L, *Science*, 281 (1998) 2019.
22 Schenk P M, *Nature*, 417 (2002) 419.
23 Nimmo F, Giese B & Pappalardo R T, *Geophys Res Lett*, 30 (2003) 37.
24 Zahnle K, Dones L & Levison H F, *Icarus*, 136 (1998) 202.
25 Squyres S W, Reynolds R T & Cassen P M, *Nature*, 301 (1983) 225.
26 Carlson R W, Calvin W M, Dalton J B, Hansen G B, Hudson R L, Johnson R E, McCord T B, & Moore M H, cited in *Europa*, Edited by Pappalardo R T, McKinnon W B & Khurana K K, (University of Arizona Press, Tucson) (2009) 283.
27 Moroz V I, *Sov Astron*, 9 (1966) 999.
28 Kuiper G P, *Astron J*, 62 (1957) 245.
29 Fink U, Dekkers N H & Larson H P, *Astrophys J Lett*, 179 (1973) L155.
30 Hansen G B & McCord T B, *J Geophys Res Planets*, 109 (2004) E01012.
31 Pollack J B, Witteborn F C, Erickson E F, Strecker D W, Baldwin B J & Bunch T E, *Icarus*, 36 (1978) 271.
32 Clark R N, *Icarus*, 44 (1980) 388.
33 Clark R N, *J Geophys Res Solid Earth*, 86 (1981) 3087.
34 Carlson R, Smythe W, Baines K, Barbinis E, Becker K, Burns R, Calcutt S, Calvin W, Clark R, Danielson G, Davies A, Drossart P, Encrenaz T, Fanale F, Granahan J, Hansen G, Herrera P, Hibbitts C, Hui J, Irwin P, Johnson T, Kamp L, Kieffer H, Leader F, Lellouch E., Lopes-Gautier R, Matson D, McCord T, Mehlman R, Ocampo A, Orton G, Roos-Serote M, Segura M, Shirley J, Soderblom L, Stevenson A, Taylor F, Torson J, Weir A & Weissman P, *Science*, 274 (1996) 385.
35 McCord T B, Hansen G B, Clark R N, Martin P D, Hibbitts C A, Fanale F P, Granahan J C, Segura M, Matson D L, Johnson T V, Carlson R W, Smythe W D, & Danielson G E, *J Geophys Res Planets*, 103 (1998) 8603.
36 McCord T B, Hansen G B, Fanale F P, Carlson R W, Matson D L, Johnson T V, Smythe W D, Crowley J K, Martin P D, Ocampo A, Hibbitts C A & Granahan J C, *Science*, 280 (1998) 1242.
37 Orlando T M, McCord T B & Grieves G A, *Icarus*, 177 (2005) 528.
38 Dalton J B, *Geophys Res Lett*, 34 (2007) L21205.
39 Brown M E & Hand K P, *Astronom J*, 145 (2013) 110.
40 Meija J, Coplen T B, Berglund M, Brand W A, Bievre P D, Groning M, Holden N E, Irrgeher J, Loss R D, Walczyk T & Prohaska T, *Pure Appl Chem*, 88 (2016) 265.
41 Krause M O, *J Phys Chem Ref Data*, 8 (1979) 307.
42 McMaster W H, Kerr Del Grande N, Mallett J H, & Hubbell J H, *At Data Nucl Data Tables*, 8 (1970) 443.
43 Bambynek W, Crasemann B, Fink R W, Freund H U, Mark H, Swift C D, Price R E & Rao P V, *Rev Mod Phys*, 44 (1972) 716.
44 Schoonjans T, Brunetti A, Golosio B, del Rio M S, Sol´e V A, Ferrero C & Vincze L, *Spectrochim Acta B*, 66 (2011) 776.
45 Berger M J & Hubbell J H, Technical Report 87-3597 (NIST, United States), 1987.
46 Mohr P J, Newell D B & Taylor B N, *J Phys Chem Ref Data*, 45 (2016) 043102.
47 Hubbell J H, Veigele W J, Briggs E A, Brown R T, Cromer D T & Howerton R J, *J Phys Chem Ref Data*, 4 (1975) 471.
48 Cromer D & Waber J, International Tables for X-ray Crystallography, The Kynoch Press: Birmingham, 4 (1974).